Received: 22 June 2023 | Revised: 26 July 2023 | Accepted: 23 August 2023

DOI: 10.1002/pamm.202300031

RESEARCH ARTICLE

Characterization of ductile damage and fracture behavior under shear reverse loading conditions

Zhichao Wei | **Steffen Gerke** | **Michael Brünig**

Institut für Mechanik und Statik, Universität der Bundeswehr München, Neubiberg, Germany

Correspondence
Zhichao Wei, Institut für Mechanik und Statik, Universität der Bundeswehr München, Werner-Heisenberg-Weg 39, D-85577 Neubiberg, Germany.
Email: zhichao.wei@unibw.de

Funding information
Deutsche Forschungsgemeinschaft, Grant/Award Number: 322157331

Abstract

This paper deals with experimental and numerical analysis of the ductile damage and fracture behavior undergoing biaxial non-proportional shear reverse loading conditions. In the numerical analysis, an anisotropic cyclic plastic-damage constitutive model is considered to characterize the damage and fracture behavior. Additionally, the change in the hardening rate is observed after shear reverse loading. Thus, a newly modified non-hardening strain region method is introduced to capture the change in the hardening ratio between isotropic and kinematic hardening. Furthermore, the damage surface is assumed to translate in the direction of the damage strain increment. Hence, a softening law based on the damage strain is proposed. The modified constitutive model predicts macroscopic force-displacement and microscopic evolution of plastic and damage behaviors under shear reverse loading with a tensile preload. Through digital image correlation technique and scanning electron microscopy, numerical results can be validated by experimental ones. Furthermore, scanning electron microscopy pictures also reveal different damage and fracture mechanisms on the micro-level.

1 | INTRODUCTION

Many experiments and numerical investigations have shown that stress states affect the ductile damage and fracture behavior of metals. However, in the last decades, studies have been limited to examining ductile damage and fracture caused by monotonic loading or one-axis-loaded reverse loading conditions [1–5]. Among them, one-axis-loaded shear monotonic and cyclic tests have shown that the coalescence of the micro-shear-cracks mainly causes ductile damage, and shear reverse loading affects the evolution of damage and fracture behavior compared to the monotonic loading [4]. On the other hand, limited studies have focused on reverse torsion loading under non-proportional loading conditions with a cylindrical specimen. In the case of metal sheets, biaxially loaded cruciform specimens have been recognized as a proficient means of generating complex stress states. For instance, Gerke et al. [6] proposed a biaxially loaded H-specimen that includes a tensile axis and shear axis to generate different stress states in different loading axes. Thus, the H-specimen enables non-proportional loading by changing the tensile preload to shear load during the experiment. Moreover, previous studies indicate that various preloading histories can induce different stress states and result in further damage

and fracture. However, the mentioned studies have been restricted to monotonic loading conditions. To fill this gap, a series of biaxial shear reverse loading with non-proportional loading tests taking into account different tensile preloads is performed for aluminum alloy sheets.

In the present work, the H-specimen is modified by increasing the distance in the central notch part to conduct the cyclic tests, the so-called HC-specimen. The experimental methodology involves a two-step loading process. Different proportional tensile preloads, without unloading, are imposed on the tensile axis at the first loading stage to generate a range of stress triaxialities. Subsequently, in the second loading stage, a three-half-shear cyclic loading is superimposed on the shear axis until fracture. By following this approach, the experimental results allow for the investigation of the damage and fracture behavior of the material under different stress states.

2 | CONSTITUTIVE MODELING

It is imperative to acknowledge that ductile metals primarily undergo significant plastic deformations before the manifestation of material degradation, commonly referred to as damage. As a result, Brünig [7] proposed a novel two-surface approach to capture large plastic and damage deformations for ductile metals. This innovative approach uses an anisotropic second-order damage strain rate tensor to predict damage evolution caused by various damage mechanisms on the micro-scale accurately. Recently, Wei et al. [4] incorporated combined hardening laws into the plasticity yield criterion to capture the plastic-damage behavior under reverse loading conditions. Additionally, a new kinematic softening model is proposed to characterize the translation of the damage surface.

For metals [4] and geomaterials [8], onset of plastic yielding is sensitive to hydrostatic pressure. Therefore, the Drucker-Prager yield criterion taking into account the combined hardening law

$$f^{\mathrm{pl}} = \sqrt{\frac{1}{2}\mathrm{dev}(\bar{\mathbf{T}} - \bar{\boldsymbol{\alpha}})\cdot\mathrm{dev}(\bar{\mathbf{T}} - \bar{\boldsymbol{\alpha}})} + \bar{c}\left[\frac{a}{\bar{c}}\,\mathrm{tr}(\bar{\mathbf{T}} - \bar{\boldsymbol{\alpha}}) - 1\right] = 0\,, \tag{1}$$

is used to accurately characterize plastic behavior, where $\bar{\mathbf{T}}$ is the effective Kirchhoff stress tensor, $\bar{\boldsymbol{\alpha}}$ represents the effective back stress tensor, and $a/\bar{c}$ is the hydrostatic stress coefficient. The current equivalent yield stress

$$\bar{c} = c_0 + Q_1(1 - e^{-p_1\gamma}) + Q_2\xi(1 - e^{-p_2\gamma}) \tag{2}$$

is given by the extended Voce hardening law with the initial yield stress c_0, the hardening moduli Q_1 and Q_2, the additional variable function ξ, the equivalent plastic strain γ as well as the hardening exponents p_1 and p_2. The rate of the effective back stress tensor

$$\dot{\bar{\boldsymbol{\alpha}}} = \sum_{i=1}^{3} \dot{\bar{\boldsymbol{\alpha}}}_i \tag{3}$$

with modified Chaboche nonlinear kinematic hardening components

$$\begin{aligned}
\dot{\bar{\boldsymbol{\alpha}}}_1 &= b_1\chi\dot{\bar{\mathbf{H}}}^{\mathrm{pl}} - b_2\chi\dot{\gamma}\bar{\boldsymbol{\alpha}}_1 \\
\dot{\bar{\boldsymbol{\alpha}}}_2 &= b_3\dot{\bar{\mathbf{H}}}^{\mathrm{pl}} - b_4\dot{\gamma}\bar{\boldsymbol{\alpha}}_2 \\
\dot{\bar{\boldsymbol{\alpha}}}_3 &= b_5\dot{\bar{\mathbf{H}}}^{\mathrm{pl}} - (1 - \cos^2\theta)b_6\dot{\gamma}\bar{\boldsymbol{\alpha}}_3\,,
\end{aligned} \tag{4}$$

is used to capture the Bauschinger effect (BE) and changes in the yield surface under reverse loading conditions, where b_1–b_6 are material constants, $\dot{\bar{\mathbf{H}}}^{\mathrm{pl}}$ is the plastic strain rate tensor, χ represents the additional variable function, and $\cos^2\theta$ denotes the angle parameter .

Furthermore, the total hardening rate

$$\dot{\bar{\sigma}} = k_h\rho_h\dot{\bar{c}} + (1 - k_h\rho_h)\dot{\bar{\alpha}} \tag{5}$$

is an additive combination of the equivalent stress rate $\dot{\tilde{c}}$ and effective back stress rate $\dot{\tilde{\alpha}}$ in terms of the isotropic hardening proportion ρ_h and the scalar factor k_h. In the previous work [4, 9], the hardening ratio ρ_h is assumed to be constant ($k_h = 1$) during the whole cyclic loading process. However, some researchers [5, 10, 11] indicated that the hardening rate changes significantly after shear reverse loading condition. Compared to the multi-surfaces [10] and multi-kinematic-hardening-parameters approach [11], the most straightforward effective hardening function

$$k_h = \begin{cases} 0 & \text{for} \quad \gamma^* \le 0.05 \quad \text{and} \quad \gamma^* < \gamma \\ 1 - e^{-60(\gamma^* - 0.05)} + (10\gamma^* - 0.5)e^{-6} & \text{for} \quad 0.05 < \gamma^* \le 0.15 \quad \text{and} \quad \gamma^* < \gamma \\ 1 & \text{for} \quad 0.15 < \gamma^* < \gamma \quad \text{or} \quad \gamma^* \ge \gamma \end{cases}, \tag{6}$$

based on a cyclic equivalent plastic strain γ^* is introduced to predict the change in hardening after shear reverse loading [12].

On the other hand, the damage criterion f^{da} taking into account combined softening law and stress invariants I_1 and J_2 is defined as

$$f^{\mathrm{da}} = \hat{\alpha}\,\mathrm{tr}(\mathbf{T} - \boldsymbol{\alpha}) + \hat{\beta}\sqrt{\frac{1}{2}\mathrm{dev}(\mathbf{T} - \boldsymbol{\alpha})\cdot\mathrm{dev}(\mathbf{T} - \boldsymbol{\alpha})} - \tilde{\sigma} = \hat{\alpha} I_1 + \hat{\beta}\sqrt{J_2} - \tilde{\sigma} = 0\,, \tag{7}$$

where $\hat{\alpha}$ and $\hat{\beta}$ are stress-state-dependent variables, $\mathbf{T}$ is the Kirchhoff stress tensor, $\boldsymbol{\alpha}$ denotes the damage back stress tensor, and $\tilde{\sigma}$ represents the initial equivalent damage stress. In addition, the rate of damage back stress tensor is formulated as

$$\dot{\boldsymbol{\alpha}} = d_1 \dot{\mathbf{H}}^{\mathrm{da}} - d_2 \dot{\mu}\boldsymbol{\alpha}\,, \tag{8}$$

where d_1 and d_2 are softening moduli, $\dot{\mu}$ is the equivalent damage strain rate, and the damage strain rate

$$\dot{\mathbf{H}}^{\mathrm{da}} = \dot{\mu}(\tilde{\alpha}\frac{1}{\sqrt{3}}\mathbf{1} + \tilde{\beta}\tilde{\mathbf{N}}) \tag{9}$$

describes the growth of voids (isotropic volumetric part) and formation of micro-shear-cracks (deviatoric part), where the stress-state-dependent variables $\tilde{\alpha}$ and $\tilde{\beta}$ and the transformed normalized deviatoric stress tensor $\tilde{\mathbf{N}} = \frac{\mathrm{dev}(\tilde{\mathbf{T}} - \tilde{\alpha})}{\sqrt{2J_2}}$ haven been used.

Furthermore, the equivalent damage stress rate

$$\dot{\sigma} = \rho_s \dot{\tilde{\sigma}} + (1 - \rho_s)\dot{\alpha}_{\mathrm{eq}}\,, \tag{10}$$

is an additive combination of the isotropic equivalent damage stress rate $\dot{\tilde{\sigma}}$ related to the size change of the damage surface and the equivalent kinematic damage back stress rate $\dot{\alpha}_{\mathrm{eq}}$ corresponding to the translation of the damage surface. ρ_s is the isotropic softening proportion, which is assumed to be constant and equals the hardening proportion ρ_h. The stress triaxiality

$$\eta = \frac{\sigma_{\mathrm{m}}}{\sigma_{\mathrm{eq}}} = \frac{I_1}{3\sqrt{3J_2}}\,, \tag{11}$$

calculated as the ratio of hydrostatic stress σ_{m} and the von Mises equivalent stress σ_{eq}, as well as the Lode parameter

$$\omega = \frac{2T_2 - T_1 - T_3}{T_1 - T_3} \quad \text{with} \quad T_1 \ge T_2 \ge T_3\,, \tag{12}$$

expressed in the principal stress components T_i, are two key parameters used to characterize the stress states in metals. Both parameters have important applications in the study of damage and fracture mechanics.

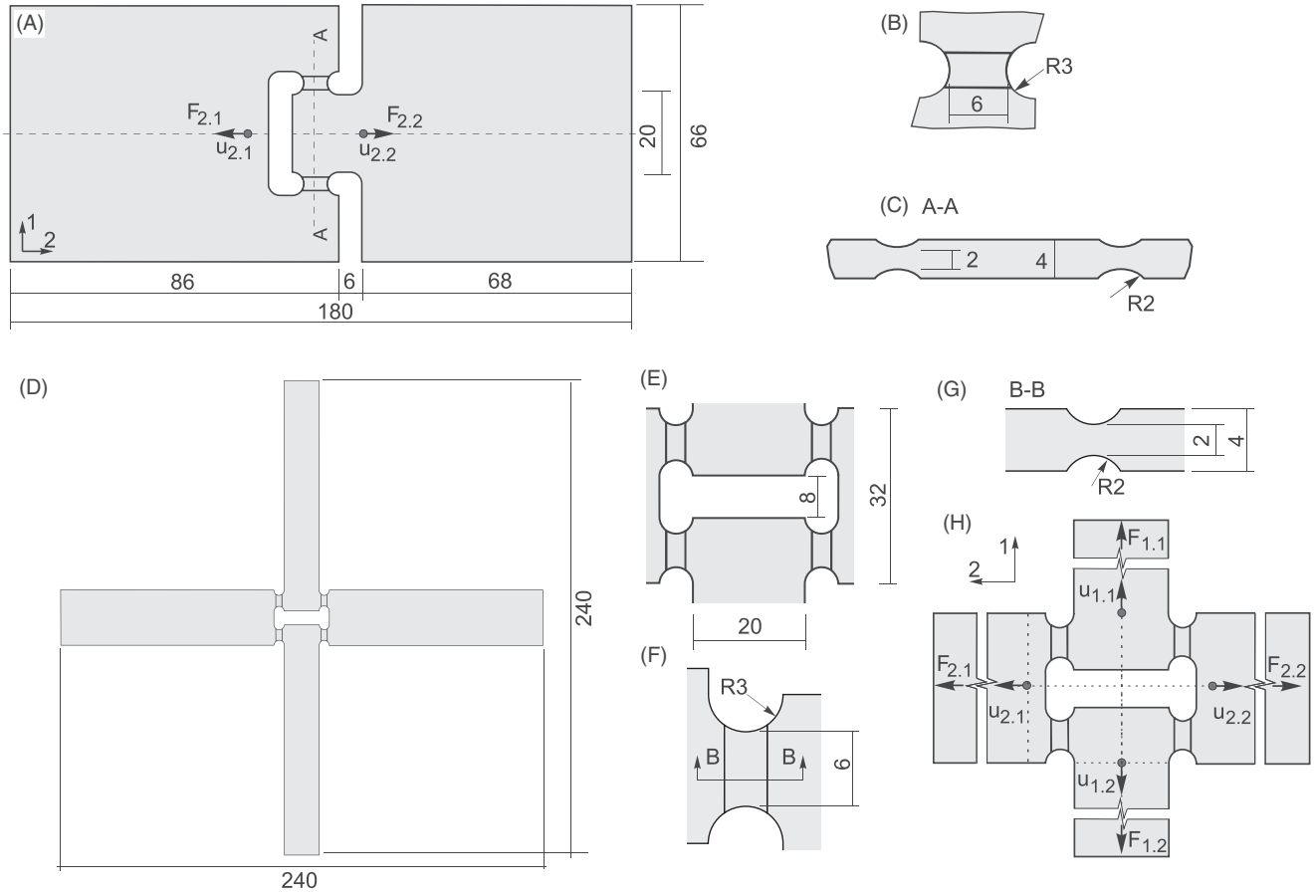

FIGURE 1 Geometries: (A)-(C) one-axis-loaded shear specimen and (D)-(H) HC-specimen; all dimensions in mm.

3 | EXPERIMENTAL SETUP AND MATERIAL PARAMETERS

The one-axis-loaded shear and HC-specimen geometries are shown in Figure 1, respectively. For the one-axis-loaded shear test, the cyclic load is imposed on the horizontal axis (axis 2, see Figure 1A), and the experimental technique can be found in ref. [4]. In the case of the non-proportional biaxial shear reverse test, the loading process is divided into two stages: in the first loading stage, preload 7 kN is imposed on the tensile axis of the HC-specimen (horizontal axis, see Figure 1H), without unloading. Subsequently, a tension-compression-tension (TCT) three-half cycle shear reverse loading is superimposed on the shear axis (vertical axis) until the specimens fail. The test is labeled cyc-T7 in this paper.

The material parameters of the investigated aluminum alloy EN-AW 6082-T6 (chemical components, see ref. [4]) are summarized in Table 1. The elastic and plastic material parameters are directly determined using the uniaxial tensile monotonic and cyclic experiments data. The parameter identification technique is discussed in detail in ref. [4, 9]. Additionally, the material constants for modeling the damage are inversely fitted based on the experiments.

4 | EXPERIMENTAL AND NUMERICAL RESULTS

The experimental force-displacement curves for the one-axis-loaded shear cyclic tests TCT and CTCT, plotted as the back dashed lines in Figure 2, have been published in ref. [4]. The corresponding numerical results without the non-hardening correction (wo/ corr., represented by blue solid lines) can also be found in ref. [4]. Moreover, the numerically predicted force-displacement curves taking into account the non-hardening correction (w/ corr.) are illustrated with the red solid lines in Figure 2. Obviously, the numerical results considering the non-hardening correction after shear reverse loading significantly improve the numerical accuracy, especially the global force-displacement behavior after reversal yielding.

Again, the experimental and numerical force-displacement curves for the test cyc-T7 are shown in Figure 3. As illus-

TABLE 1 Material parameters.

Symbol	Description	Value	Unit
E	E-modulus	67500	MPa
ν	Poisson's ratio	0.29	–
$\eta_1 \dots \eta_4$	Elastic damage moduli	−10000	MPa
c_0	Initial yield stress	139	MPa
Q_1	Isotropic hardening modulus	74.93	MPa
Q_2	Isotropic hardening modulus	21.32	MPa
p_1	Isotropic hardening exponent	8.96	–
p_2	Isotropic hardening exponent	676.01	–
$^{a}/_{c}$	Hydrostatic stress coefficient	32	$^{1}/_{\mathrm{TPa}}$
b_1	Kinematic hardening modulus	61250	MPa
b_2	Kinematic hardening constant	1750	–
b_3	Kinematic hardening modulus	895	MPa
b_4	Kinematic hardening constant	15	–
b_5	Kinematic hardening modulus	115	MPa
b_6	Kinematic hardening constant	7.5	–
ρ_h	Isotropic hardening proportion	0.41	–
$\tilde{\sigma}_0$	Initial equivalent damage stress	270	MPa
C_1	Isotropic softening modulus	0.004207	MPa
C_2	Isotropic softening exponent	92.97	–
d_1	Kinematic softening modulus	−0.51	MPa
d_2	Kinematic softening constant	−84	–
ρ_s	Isotropic softening proportion	0.41	–

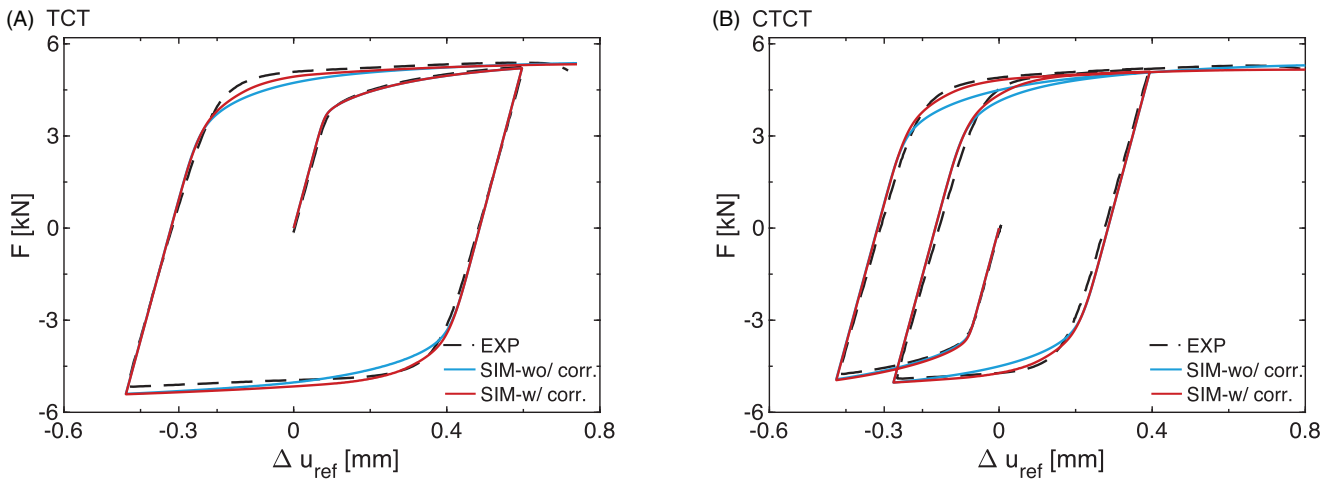

FIGURE 2 Numerical and experimental force-displacement curves for one-axis-loaded shear tests.

trated in Figure 3A, it is evident that the numerically predicted force-displacement curve without the non-hardening correction fails to accurately capture the experimental behavior, especially in the last tensile loading pattern. The proposed non-hardening correction can justify this behavior, providing a more accurate numerical result, as shown in Figure 3B. In addition, the changes of the first principal strains A_1 on the notch surface during the cyclic loading processes (RP1, RP2, and FP) are displayed in Figure 4A. The first principal strains A_1 at reverse point 1 (RP1) and fracture point (FP) are distributed in the form of a left-sloping shear band and localized on the notch surface left-top and right-bottom with maximum values of 0.1089 and 0.265, respectively, as observed in Figure 4A. At reverse point 2 (RP2), the first principal strain A_1 is distributed as an x-shape, and their maximum value equals 0.110. It indicates that the reverse loading histories

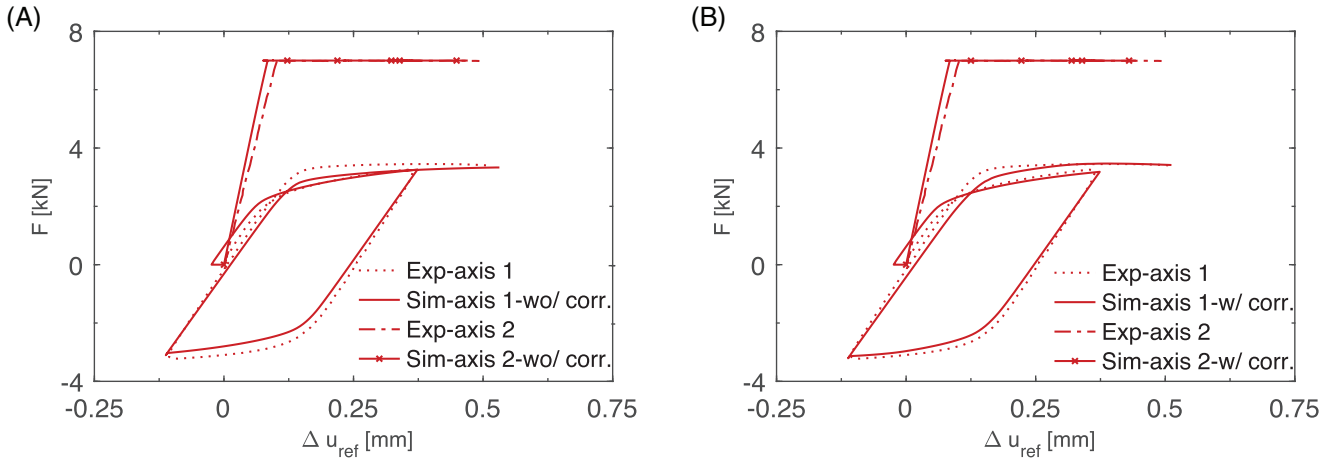

FIGURE 3 Numerical and experimental force-displacement curve for the test cyc-T7.

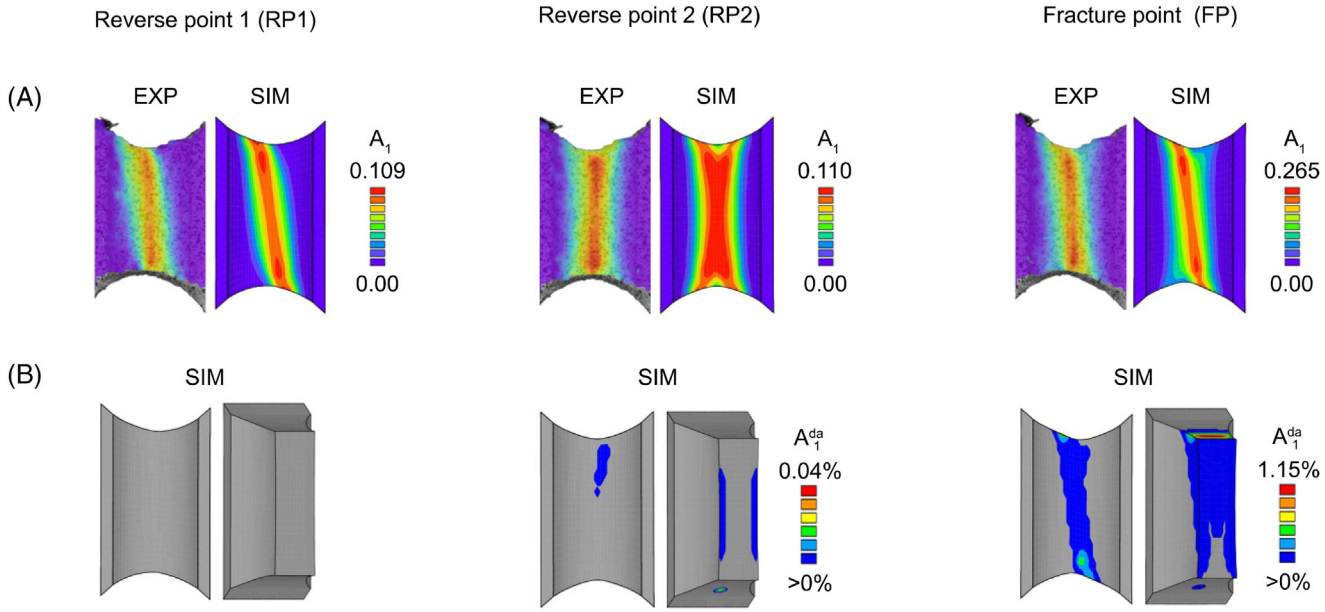

FIGURE 4 The first principal strains A_1 and the first principal damage strains A_1^{da}.

change the distribution of the first principal strains and affect the associated plastic behavior. Moreover, the evolution of the first principal damage strains A_1^{da} during the loading processes is shown in Figure 4A. No damage appears at RP1. During the subsequent reverse loading, the first principal damage strains A_1^{da} are observed in the notched surface and the notch cross-section, where the maximum value $A_1^{da} = 0.04\%$ is numerically predicted on the bottom of the notched surface. Finally, the damage occurs and develops on the notched surface induced by a positive shear loading pattern, resulting in the maximum first principal damage strain $A_1^{da} = 1.15\%$ at the top edge of the notched surface. In conclusion, shear reverse loading conditions change strain states during the experiments and significantly influence the evolution of damage.

Figure 5 shows the fractured picture and the scanning electron microscopy image taken from the fractured surface. As seen in Figure 5A, the specimen breaks in the right-top and left-bottom of the notches, and the distribution of the fracture line is consistent with the distribution of the first principal strain in Figure 4A (FP). In addition, large voids and coalesced micro-shear-cracks are visible in Figure 5B since a high stress-triaxiality ($\eta = 0.48$, $\omega = -0.65$) is numerically predicted in the test cyc-T7. As pointed out in ref. [4], the one-axis-loaded shear cyclic tests generate stress triaxialities from −0.1 to 0.1. Thus, the novel non-proportional biaxial tests enable different stress states to study the influence of shear reverse loading conditions on plastic, damage, and fracture behavior.

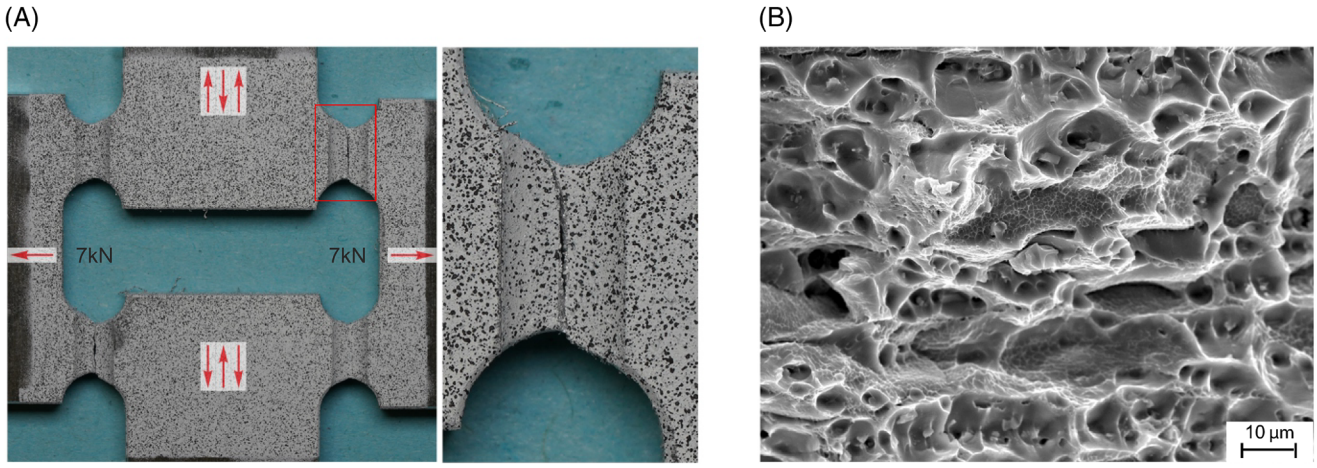

FIGURE 5 Fracture picture and scanning electron microscopy image.

5 | CONCLUSIONS

Biaxially loaded non-proportional shear reverse experiments using cruciform flat HC-specimens are performed to investigate the plastic, damage, and fracture behavior in ductile metal sheets. In addition, an anisotropic damage model considering the BE, the strength-differential effect, and the change in the hardening ratio under shear reverse loading is proposed to capture the material behavior in both macro- and micro-levels. The numerically predicted global force-displacement curves, as well as the local strain fields, agree with the experimental results. Most importantly, the proposed non-hardening corrections significantly improve the numerical results. Moreover, the numerical and experimental analysis show that the different preloads significantly affect the plastic, damage, and fracture behavior. In future work, the effect of a wide range of preloads will be investigated in further experiments.

ACKNOWLEDGMENTS

The authors gratefully acknowledge financial support of the Deutsche Forschungsgemeinschaft (DFG, German Research Foundation) – project number 322157331.

Open access funding enabled and organized by Projekt DEAL.

ORCID

Zhichao Wei https://orcid.org/0000-0002-5002-6415
Steffen Gerke https://orcid.org/0000-0003-2261-3855
Michael Brünig https://orcid.org/0000-0002-6338-4238

REFERENCES

1. Kanvinde, A. M., & Deierlein, G. G. (2007). Cyclic void growth model to assess ductile fracture initiation in structural steels due to ultra low cycle fatigue. *Journal of Engineering Mechanics*, *133*(6), 701–712.
2. Voyiadjis, G. Z., Hoseini, S. H., & Farrahi, G. H. (2013). A plasticity model for metals with dependency on all the stress invariants. *Journal of Engineering Materials and Technology*, *135*(1), 011002.
3. Algarni, M., Bai, Y., Zwawi, M., & Ghazali, S. (2019). Damage evolution due to extremely low-cycle fatigue for Inconel 718 alloy. *Metals*, *9*(10), 1109.
4. Wei, Z., Zistl, M., Gerke, S., & Brünig, M. (2022). Analysis of ductile damage and fracture under reverse loading. *International Journal of Mechanical Sciences*, *228*, 107476.
5. Daroju, S., Kuwabara, T., Sharma, R., Fullwood, D. T., Miles, M. P., & Knezevic, M. (2022). Experimental characterization and crystal plasticity modeling for predicting load reversals in AA6016-T4 and AA7021-T79. *International Journal of Plasticity*, *153*, 103292.
6. Gerke, S., Adulyasak, P., & Brünig, M. (2017). New biaxially loaded specimens for the analysis of damage and fracture in sheet metals. *International Journal of Solids and Structures*, *110*, 209–218.
7. Brünig, M. (2003). An anisotropic ductile damage model based on irreversible thermodynamics. *International Journal of Plasticity*, *19*(10), 1679–1713.

8. Zhang, J., Brepols, T., & Reese, S. (2023). A two–surface damage–plasticity model based on a Drucker—Prager yield criterion. *Proceedings in Applied Mathematics and Mechanics*, *22*(1), e202200296.
9. Wei, Z., Zistl, M., Gerke, S., & Brünig, M. (2023). Analysis of ductile damage evolution and failure mechanisms due to reverse loading conditions for the aluminum alloy EN-AW 6082-T6. *Proceedings in Applied Mathematics and Mechanics*, *22*(1), e202200012.
10. Ohno, N. (1982). A constitutive model of cyclic plasticity with a nonhardening strain region. *Journal of Applied Mechanics*, *49*(4), 721–727.
11. Okorokov, V., Gorash, Y., Mackenzie, D., & van Rijswick, R. (2019). New formulation of nonlinear kinematic hardening model, part I: a Dirac delta function approach. *International Journal of Plasticity*, *122*, 89–114.
12. Wei, Z., Gerke, S., & Brünig, M. (2023). Damage and fracture behavior under non-proportional biaxial reverse loading in ductile metals: experiments and material modeling (submitted). *International Journal of Plasticity.*

How to cite this article: Wei, Z., Gerke, S., & Brünig, M. (2023). Characterization of ductile damage and fracture behavior under shear reverse loading conditions. *Proceedings in Applied Mathematics and Mechanics*, *23,* e202300031. https://doi.org/10.1002/pamm.202300031